arXiv:1707.05630v3 [physics.ins-det] 26 Sep 2017

Simulation of argon response and light detection in the DarkSide-50 dual phase TPC

P. Agnes[a] I. F. M. Albuquerque[b] T. Alexander[c] A. K. Alton[d] D. M. Asner[c] H. O. Back[c]
K. Biery[e] V. Bocci[f] G. Bonfini[g] W. Bonivento[h] M. Bossa[i,g] B. Bottino[j,k] F. Budano[l,m]
S. Bussino[l,m] M. Cadeddu[n,h] M. Cadoni[n,h] F. Calaprice[o] N. Canci[a,g] A. Candela[g]
M. Caravati[n,h] M. Cariello[k] M. Carlini[g] S. Catalanotti[p,q] V. Cataudella[p,q] P. Cavalcante[r,g]
A. Chepurnov[s] C. Cicalò[h] A. G. Cocco[q] G. Covone[p,q] D. D'Angelo[t,u] M. D'Incecco[g]
S. Davini[k,i] A. de Candia[p,q] S. De Cecco[v] M. De Deo[g] G. De Filippis[p,q] M. De Vincenzi[l,m]
A. V. Derbin[w] G. De Rosa[p,q] A. Devoto[n,h] F. Di Eusanio[o] G. Di Pietro[g,u] C. Dionisi[f,v]
E. Edkins[x] A. Empl[a] A. Fan[y] G. Fiorillo[p,q] K. Fomenko[z] D. Franco[aa] F. Gabriele[g]
C. Galbiati[o,u] S. Giagu[f,v] C. Giganti[ab] G. K. Giovanetti[o] A. M. Goretti[g] F. Granato[ac]
M. Gromov[s] M. Guan[ad] Y. Guardincerri[e] B. R. Hackett[x] K. Herner[e] D. Hughes[o] P. Humble[c]
E. V. Hungerford[a] An. Ianni[o,g] I. James[l,m] T. N. Johnson[ae] K. Keeter[af] C. L. Kendziora[e]
G. Koh[o] D. Korablev[z] G. Korga[a,g] A. Kubankin[ag] X. Li[o] M. Lissia[h] B. Loer[c] G. Longo[p,q]
Y. Ma[ad] A. A. Machado[ah] I. N. Machulin[ai,aj] A. Mandarano[i,g] S. M. Mari[l,m] J. Maricic[x]
C. J. Martoff[ac] P. D. Meyers[o] R. Milincic[x] A. Monte[ak] B. J. Mount[af] V. N. Muratova[w]
P. Musico[k] J. Napolitano[ac] A. Navrer Agasson[ab] A. Oleinik[ag] M. Orsini[g] F. Ortica[al,am]
L. Pagani[ae] M. Pallavicini[j,k] E. Pantic[ae] K. Pelczar[g] N. Pelliccia[al,am] A. Pocar[ak] S. Pordes[e]
D. A. Pugachev[ai] H. Qian[o] K. Randle[o] M. Razeti[h] A. Razeto[g,o] B. Reinhold[x] A. L. Renshaw[a]
M. Rescigno[f] Q. Riffard[aa] A. Romani[al,am] B. Rossi[q] N. Rossi[g] D. Sablone[o,g] W. Sands[o]
S. Sanfilippo[l,m] C. Savarese[i,g] B. Schlitzer[ae] E. Segreto[ah] D. A. Semenov[w] P. N. Singh[a]
M. D. Skorokhvatov[ai,aj] O. Smirnov[z] A. Sotnikov[z] C. Stanford[o] Y. Suvorov[y,g,ai] R. Tartaglia[g]
G. Testera[k] A. Tonazzo[aa] P. Trinchese[p,q] E. V. Unzhakov[w] M. Verducci[f,v] A. Vishneva[z]
B. Vogelaar[r] M. Wada[o] S. Walker[p,q] H. Wang[y] Y. Wang[ad,y] A. W. Watson[ac] S. Westerdale[o]
J. Wilhelmi[ac] M. M. Wojcik[an] X. Xiang[o] X. Xiao[y] C. Yang[ad] Z. Ye[a] C. Zhu[o] G. Zuzel[an]

[a]Department of Physics, University of Houston, Houston, TX 77204, USA

[b]Instituto de Física, Universidade de São Paulo, São Paulo 05508-090, Brazil

[c]Pacific Northwest National Laboratory, Richland, WA 99352, USA

[d]Physics Department, Augustana University, Sioux Falls, SD 57197, USA

[e]Fermi National Accelerator Laboratory, Batavia, IL 60510, USA

[f]INFN Sezione di Roma, Roma 00185, Italy

[g]INFN Laboratori Nazionali del Gran Sasso, Assergi (AQ) 67100, Italy

[h]INFN Cagliari, Cagliari 09042, Italy

[i]Gran Sasso Science Institute, L'Aquila 67100, Italy

[j]Physics Department, Università degli Studi di Genova, Genova 16146, Italy

[k]INFN Genova, Genova 16146, Italy

[l] INFN Roma Tre, Roma 00146, Italy

[m] Mathematics and Physics Department, Università degli Studi Roma Tre, Roma 00146, Italy

[n] Physics Department, Università degli Studi di Cagliari, Cagliari 09042, Italy

[o] Physics Department, Princeton University, Princeton, NJ 08544, USA

[p] Physics Department, Università degli Studi "Federico II" di Napoli, Napoli 80126, Italy

[q] INFN Napoli, Napoli 80126, Italy

[r] Virginia Tech, Blacksburg, VA 24061, USA

[s] Skobeltsyn Institute of Nuclear Physics, Lomonosov Moscow State University, Moscow 119991, Russia

[t] Physics Department, Università degli Studi di Milano, Milano 20133, Italy

[u] INFN Milano, Milano 20133, Italy

[v] Physics Department, Sapienza Università di Roma, Roma 00185, Italy

[w] Saint Petersburg Nuclear Physics Institute, Gatchina 188350, Russia

[x] Department of Physics and Astronomy, University of Hawai'i, Honolulu, HI 96822, USA

[y] Physics and Astronomy Department, University of California, Los Angeles, CA 90095, USA

[z] Joint Institute for Nuclear Research, Dubna 141980, Russia

[aa] APC, Université Paris Diderot, CNRS/IN2P3, CEA/Irfu, Obs de Paris, USPC, Paris 75205, France

[ab] LPNHE, Université Pierre et Marie Curie, CNRS/IN2P3, Sorbonne Universités, Paris 75252, France

[ac] Physics Department, Temple University, Philadelphia, PA 19122, USA

[ad] Institute of High Energy Physics, Beijing 100049, China

[ae] Department of Physics, University of California, Davis, CA 95616, USA

[af] School of Natural Sciences, Black Hills State University, Spearfish, SD 57799, USA

[ag] Radiation Physics Laboratory, Belgorod National Research University, Belgorod 308007, Russia

[ah] Physics Institute, Universidade Estadual de Campinas, Campinas 13083, Brazil

[ai] National Research Centre Kurchatov Institute, Moscow 123182, Russia

[aj] National Research Nuclear University MEPhI, Moscow 115409, Russia

[ak] Amherst Center for Fundamental Interactions and Physics Department, University of Massachusetts, Amherst, MA 01003, USA

[al] Chemistry, Biology and Biotechnology Department, Università degli Studi di Perugia, Perugia 06123, Italy

[am] INFN Perugia, Perugia 06123, Italy

[an] M. Smoluchowski Institute of Physics, Jagiellonian University, 30-348 Krakow , Poland

E-mail: pagnes@in2p3.fr, dfranco@in2p3.fr

ABSTRACT: A Geant4-based Monte Carlo package named G4DS has been developed to simulate the response of DarkSide-50, an experiment operating since 2013 at LNGS, designed to detect WIMP interactions in liquid argon. In the process of WIMP searches, DarkSide-50 has achieved two fundamental milestones: the rejection of electron recoil background with a power of $\sim 10^7$, using the pulse shape discrimination technique, and the measurement of the residual ^{39}Ar contamination in underground argon, ~ 3 orders of magnitude lower with respect to atmospheric argon. These results rely on the accurate simulation of the detector response to the liquid argon scintillation, its ionization, and electron-ion recombination processes. This work provides a complete overview of the DarkSide Monte Carlo and of its performance, with a particular focus on PARIS, the custom-made liquid argon response model.

Contents

1 Introduction

Evidence from several astronomical observations and calculations shows gravitational patterns in the universe which require interactions between baryonic matter and a different form of non-luminous matter. This "dark matter" is a new form of matter that interacts gravitationally, but not via electromagnetic or strong forces, with baryons. A candidate for this dark matter is the Weakly Interacting Massive Particle, WIMP, which would exist in all gravitationally bound clusters of matter. Many searches for the existence of WIMPs are currently being performed.

Experiments looking for the direct detection of dark matter attempt to observe the recoil of an atomic nucleus which has undergone a weak interaction with a WIMP. A large number of direct dark matter searches and related R&D efforts are currently in progress, which demonstrate the present importance of this topic. Several detector types using different techniques are either acquiring data or under development in various underground laboratories. In order to identify signals which are due to non-standard, extremely rare interactions, these detectors all share the common requirements of sensitivity to the very low-energy deposition occurring in a WIMP-nuclear collision and the ability to discriminate against common, naturally occurring backgrounds.

The best WIMP-nuclear cross section limits for WIMP masses larger than 10 GeV are achieved with dual-phase, noble–liquid time projection chambers (TPC) [1–3]. Noble liquids are attractive targets for rare low energy particle interactions because of their potential radio-purity, their high

density, and their response to various particle interactions. In a dual–phase TPC, scintillation photons and ionization electrons, emitted during a WIMP-nucleus interaction, can both be detected with high resolution. The scintillation light (S1) from this interaction is detected by photosensors, while the ionization electrons drift under the influence of an electric field into a gas phase at the top of the detector where they are extracted. The extracted electrons produce a secondary pulse of light (S2) by electroluminescence in the gas. The S1 and S2 pulses provide all the necessary information needed to reconstruct the position of the interaction vertex, and aid the identification and discrimination of background events.

Liquid argon (LAr) excitation occurs with two dimer states having lifetimes differing by 2-3 orders of magnitude. The relative ratio between the two dimers is governed by the density of the energy loss due to the ionizing particle. Therefore the ratio differs for excitations due to electron as opposed to nuclear recoils, and thus the S1 pulse shape is determined by the nature of the interacting particle. This provides extraordinary discrimination between nuclear (WIMP-induced), and electron recoils.

DarkSide-50 uses a 46 kg active–mass, dual–phase argon TPC which is installed at LNGS and has been in operation since 2013. It has recently confirmed the exceptional pulse shape discrimination (PSD) of LAr [4] by identifying and rejecting approximately $1.5{\times}10^7$ electron recoil events, mainly due to ^{39}Ar decays. The ^{39}Ar component is a cosmogenically produced background which is naturally present in argon extracted from the atmosphere. Despite the large PSD power, the intrinsic ^{39}Ar contamination (~1 Bq/kg with 269 yr half-life) is so high that it prevents using atmospheric argon in a large volume experiment. The DarkSide collaboration recently overcame this problem by extracting argon from deep underground [5], which is naturally shielded from cosmic rays and hence depleted in ^{39}Ar. DarkSide-50, which was filled with underground argon in April 2015, measured a ^{39}Ar depletion factor of ~1400 [5]. This result is fundamental to the proposed DarkSide-20k (DS-20k) detector, which will use some 20 tonne of Ar depleted in ^{39}Ar. The operation of DS-20k is foreseen to start in 2020.

The success of DarkSide-50 strongly relies on a full understanding of the detector response, and this is possible thanks to detailed and accurate descriptions of the geometry, material properties, and physical processes as simulated in a Geant4–based DarkSide Monte Carlo simulation toolkit, G4DS (GEANT4.10.0.0 [6]). G4DS plays a pivotal role in the DarkSide-50 analysis, and reproduces data with high accuracy. This paper provides a full description of G4DS and of the custom physics process developed to describe the physics of the S1 and S2 signals by calibrating it with DarkSide-50 data.

2   The DarkSide-50 detector

As shown in Figure 1, the DarkSide-50 target mass of LAr (46.4±0.7 kg) is contained in a cylindrical region, laterally confined by a 2.54 cm–thick PTFE reflector, and viewed by a two arrays of 19 low-background Hamamatsu R11065 3" photomultiplier tubes (PMTs) at the top and bottom of the TPC. The quantum efficiency of the PMTs is 34 % at 420 nm, and they are entirely immersed in LAr. They view the TPC interior through fused–silica windows, which are coated on both faces by 15 nm thick conductive indium tin oxide (ITO) films. The ITO serves as a grounded anode at the top and a HV cathode at the bottom of the TPC. The windows and the radial-defining PTFE are coated

with tetraphenyl butadiene (TPB), which converts "128" nm Ar scintillation photons into 420 nm photons, so that signals are detectable by the PMTs. The electron drift system consists of the ITO cathode and anode planes, a radial field cage, and a grid used to extract drifting electrons into the 1 cm gaseous region above the LAr. The grid lies 5 mm below the liquid surface and is a hexagonal mesh which is etched from a 50 μm-thick stainless steel foil and has an optical transparency of 95% at normal incidence. The field cage lies outside the cylindrical PTFE wall and consists of copper rings held at a graded potential. It is designed to keep the drift field a uniform 200 V/cm throughout the active volume.
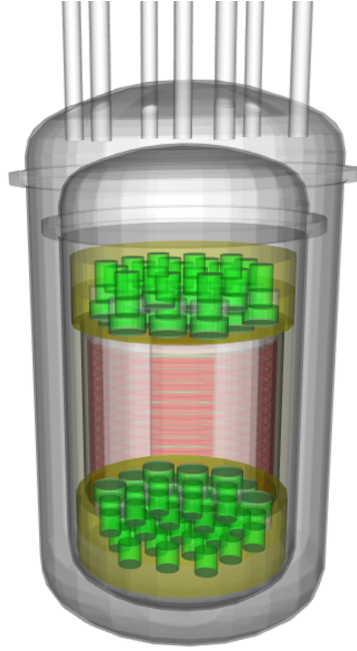

Figure 1. Simulated TPC geometry.

There are two independent, active veto shields enclosing the TPC. The outer shield is 1,000–tonne water Cherenkov muon veto with an inner, 30–tonne liquid scintillator neutron veto, as shown in Figure 2. G4DS provides a full simulation of the two vetoes, however details are omitted here since the scope of this work is limited to the simulation of the TPC. More details on the LAr TPC, the liquid scintillator veto, and the water Cherenkov veto can be found in references [4, 7, 8].

3   The Monte Carlo simulation

3.1   G4DS - Geant4-based DarkSide Monte Carlo simulation toolkit

G4DS is designed with a modular architecture in order to include a full description of all the detectors belonging to the DarkSide program. These detectors are DarkSide-10 [9], DarkSide-50 [4], DarkSide-20k [10, 11], and ARGO [12]. The last step in this experimental program will have several hundred tonnes of fiducial mass and will be able to reach the detection sensitivity required to observe solar neutrino signals, the so–called "neutrino floor".

This paper is focused on the performance of G4DS for DarkSide-50, where it plays a fundamental role in the definition of the data selection criteria, estimation of associated efficiencies,
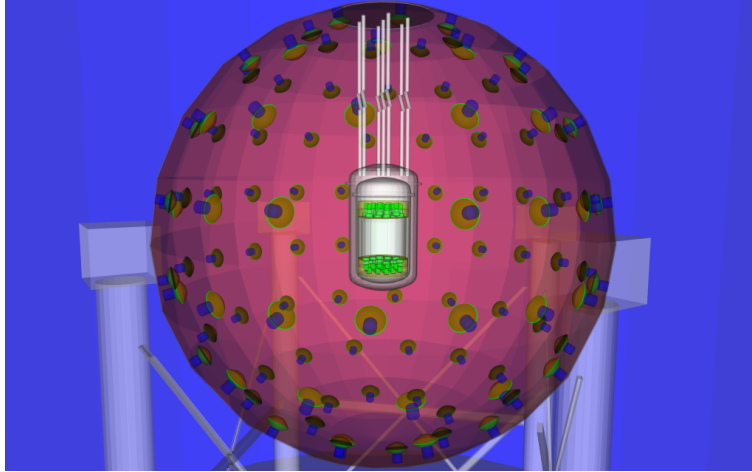
Figure 2. Simulated geometry of the TPC inside the LSV.

optimization of reconstruction algorithms, and evaluation of residual backgrounds. G4DS embeds a rich set of particle generators, detailed geometry descriptions, properly tuned physical processes, and the full optical propagation of photons produced by scintillation in liquid argon and electroluminescence in gaseous argon. It tracks all the generated photons until they reach the active region of the photosensors, where they are converted, after stochastically surviving a quantum efficiency cut, into photoelectrons. The conversion of a photoelectron into a charge signal is then handled by electronic simulation, as described in Subsection 3.2.

A large choice of event generators allows simulations of forbidden beta decays (for example ^{39}Ar and ^{85}Kr), single and chain radioactive decays, cosmic muon and neutron fluxes as measured at LNGS, and AmBe and AmC neutron calibration sources. The electromagnetic physics list used in G4DS is *G4EmLivermore*, whose lower threshold at 250 eV perfectly matches the energy range and accuracy required by DarkSide-50. The hadronic processes rely on a custom-made physics list, including the *High Precision Neutron* (HP) models for simulations of neutrons with energy lower than 20 MeV. In this range, the most dangerous background is due to neutrons induced by (α, n) and fission reactions. These neutrons are generated with the TALYS [13] package. At higher energies, an *ad hoc* FLUKA [14, 15] simulation code was implemented to study the production rates of secondary particles and nuclei induced by cosmic ray interactions. G4DS embeds generators to read and track both TALYS and FLUKA outputs.

A critical aspect of the DarkSide-50 simulation is in treating the degeneracies that arise because the LAr scintillation response is non-ŋlinear in the presence of an electric field and the light collection efficiency varies over the volume of the detector. The efficiency of light collection depends on the optical properties of materials and surfaces in the TPC. These properties have to be tuned based on observables which are independent of particle type and event energy in order to avoid degeneracies with the LAr energy response. Among the variables used for the optical tuning, described in Section 4, are PMT channel occupancies and asymmetries between the light collection in the top and bottom arrays of PMT's.

Once the optical properties are properly constrained, the DarkSide-50 energy response depends only on the processes responsible for light emission in liquid and gaseous argon. These processes

are modelled in a custom-made Geant4 module called Precision Argon Response Ionization and Scintillation (PARIS), which will be described in detail in Section 5. The PARIS module relies on the effective description of the recombination of electrons with ions, which induces a depletion of S2 in favor of the S1 signal.
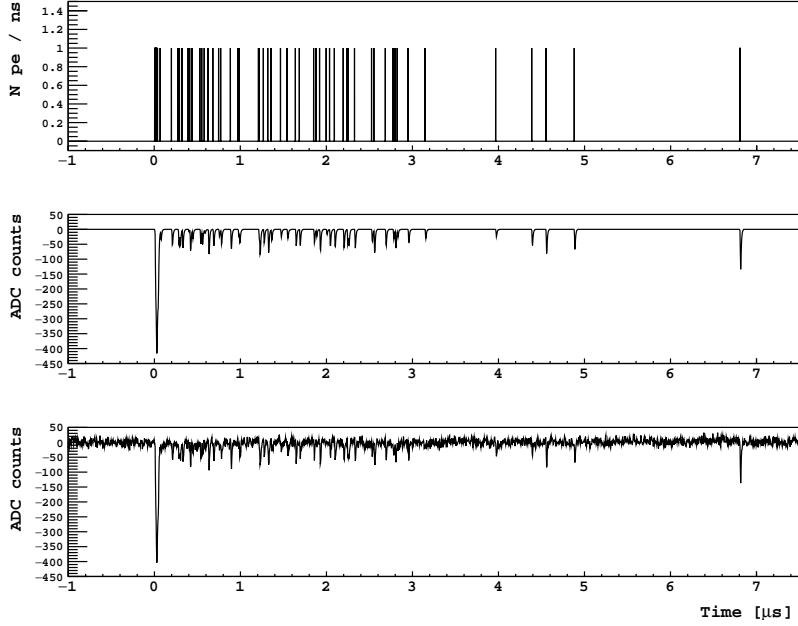
3.2 Simulation of the electronics and event reconstruction

Figure 3. Example of a waveform produced by the full Monte Carlo chain. Top: time distribution of photoelectrons generated by G4DS; middle: convolution with the PMT response; bottom: final waveform including noise extracted from real data.

The electronics simulation is developed within *DarkArt*, the `art`-based framework [16] that serves as the reconstruction code for DarkSide-50. The *DarkArt* simulation module generates waveforms for each PMT channel based on the arrival time of the photoelectrons produced by G4DS. Each photoelectron is converted into time and charge, using a single electron response (SER) that is extracted from data. The electronic noise is measured with dedicated data campaigns using a random trigger and is directly added to each simulated PMT waveform. An example of a waveform reconstructed with this procedure is shown in figure 3.

The simulated waveforms are then processed by the reconstruction code, which subtracts the baseline, identifies pulses, and integrates the charge. The difference between the reconstructed S1 variable and the true number of photoelectrons generated by G4DS is ∼1.1%, as shown in figure 4. The smearing introduced by the electronics and the reconstruction algorithms is estimated to be 5.3%, and is negligible compared to the SER.
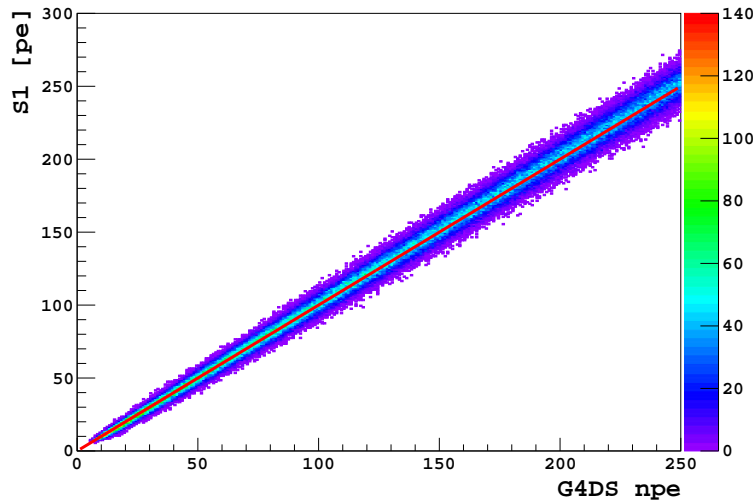
Figure 4. Reconstructed S1 as function of the true number of photoelectrons generated by G4DS. The deviation from linearity (red line) is estimated at 1.1%.

3.3 Fast Mode Approach

The full simulation of the DarkSide-50 data, including the optical propagation of S1 and S2 photons, electronics simulation, and reconstruction, is CPU and time consuming. To overcome this problem, several DarkSide-50 analyses rely on a fast reconstruction code based on the G4DS measured variables. This code stores the visible energy proportional to S2 but does not generate the S2 photons, and bypasses *DarkArt*. It reduces the simulation time by a factor of ~100 and is labelled the Fast Mode Approach (FMA). The electronics and reconstruction response for S1 can be simply modelled by smearing the number of photoelectrons with a Gaussian resolution, embedding the effects from SER, noise, and signal reconstruction. The main issue with this approach is the identification of multiply scattered events which rely on the reconstruction of multiple S2 pulses. The efficiency of the DarkSide-50 pulse finder algorithm [4] in distinguishing overlapping S2 pulses from multi-sited depositions, depends primarily on the time difference between the pulses, and hence on the spatial distance (Δz) along the drift field between the deposits.

The FMA approach implements a *clustering* algorithm, which defines a *cluster* as a set of energy depositions, whose positions along the drift field are too close to be disentangled as separate S2 pulses. The cluster position is defined as the energy-weighted average position of energy depositions. The cluster energy is the sum of the depositions, with each independently subject to recombination, as will be described in Section 5.

The minimum distance (Δz_{min}) between deposits allowing resolution of clusters was tuned using data from ^{133}Ba and ^{57}Co sources, which were located in the liquid scintillator veto close to the cryostat. These two sources are characterized by emission of 356 keV and 122 keV gamma lines, respectively. These reach the active volume after crossing the cryostat, the TPC wall, and the LAr bath surrounding the TPC. The distributions of S2 pulses identified reconstructing ^{133}Ba and ^{57}Co calibration data are compared in figure 5 with simulations processed by the FMA for different Δz_{min}.
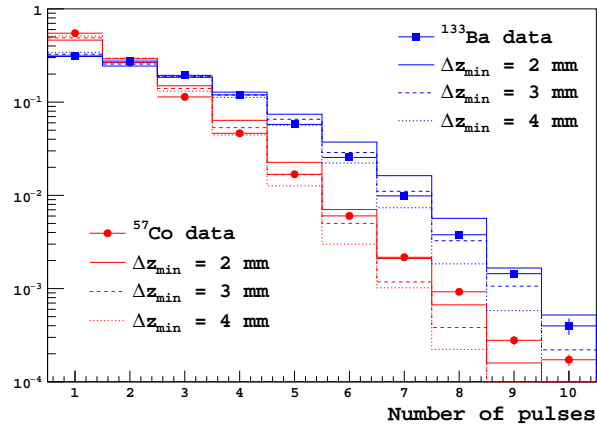
Figure 5. Comparison between the number of S2 pulses between DarkSide-50 calibration data and G4DS using the FMA reconstruction for different Δz_{min} values.
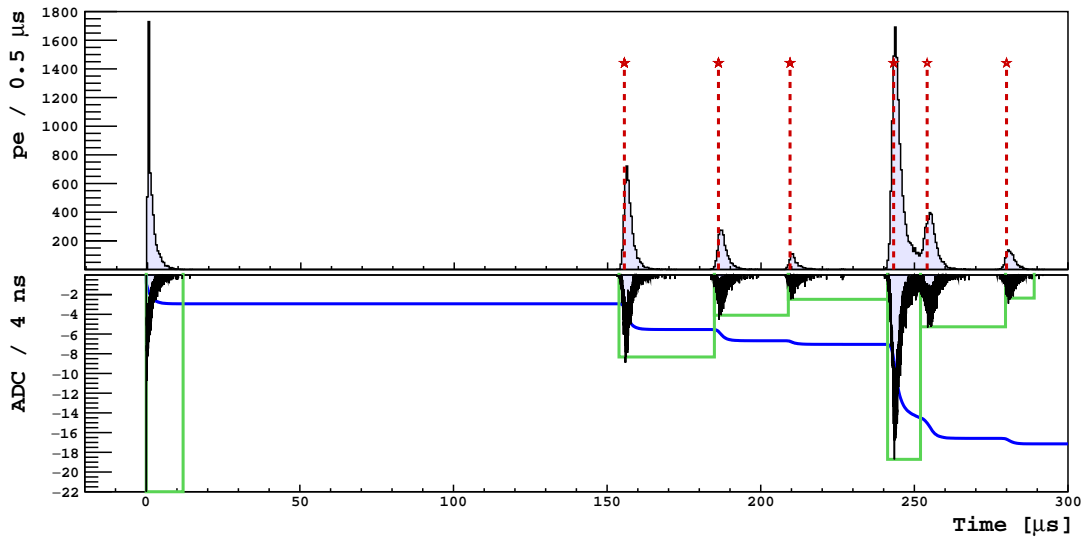

Figure 6. Comparison between the G4DS *fast* (top) and *full* (bottom) reconstruction modes for a single event. TOP: the S1 pulse (the first), followed by 6 S2 pulses, simulated with G4DS, are overlapped by dashed red lines corresponding to the pulses identified in the fast mode. BOTTOM: simulated waveform of the event (black), cumulative distribution (blue line), and the pulses (green boxes) identified by the full reconstruction mode.

The simultaneous fit of the numbers of S2 pulses of ^{133}Ba and ^{57}Co data, results in Δz_{min}=3.5 mm corresponding to a time separation of 3.8 μs assuming the drift velocity of 0.93 mm/μs [4]. The FMA clustering algorithm is also able to identify, with good accuracy, the starting time of each pulse, defined as the time of the first deposit occurring in the cluster. This is shown in Figure 6, where FMA pulses (dashed red lines) are compared for a single event with those (green boxes) identified by the *DarkArt* full reconstruction approach.

4 The Liquid Argon TPC optics

The propagation of photons from their generation in liquid or gaseous argon to the photosensor, depends on a large number of optical properties of the detector materials and their interfaces. The relevant materials affecting the simulation are the liquid and gaseous argon, the fused silica windows, the TPB coatings on each internal surface, the Indium-Tin-Oxide (ITO) electrodes, the PTFE reflectors defining the radial edge of the TPC, the grid, and the PMT windows. The sequence of materials crossed by a photon from the center of the TPC to the top, bottom, and radial sides is listed in Table 1.

Id	Up	Down	Side
1	Liquid argon	Liquid argon	Liquid argon
2	Grid	TPB	TPB
3	Liquid argon	ITO	PTFE
4	Gaseous argon	Fused silica	
5	Condensed liquid argon	ITO	
6	TPB	Liquid argon	
7	ITO	PMT cathode or PTFE	
8	Fused silica		
9	ITO		
10	Liquid argon		
11	PMT cathode or PTFE		

Table 1. Sequences of materials crossed by a photon from the center toward the top, bottom, and side of the TPC.

Most of these relevant materials are modelled as pure dielectrics, with the exceptions of the ITO coating and the grid, which are described as optical surfaces, and the PTFE which is assumed metallic, i.e a surface which photons cannot penetrate. The model for the grid, adjusted to optimize CPU simulation time, is an optical surface with a transmittance dependent on the incident photon angle. This is equal to ~95% for normal incidence. Non-transmitted photons undergo either reflection or absorption depending on a wavelength dependent function.

The ITO coating has a refractive index with an imaginary (absorptive) component, and requires a custom model. Here, reflectivity is assumed specular, and transmittance and absorbance are described as a function of the wavelength and the material on which the ITO is deposited. Figure 7 shows three optical couplings for 420 nm photons as a function of the incident angle for photons on ITO deposited on fused silica in LAr.

All the internal PTFE radial surfaces are coated with a TPB wavelength shifter. No reflection coefficients are required for the PMT supports as these are not directly exposed to the UV light due to limitations imposed by the TPB coated fused silica windows. The PTFE is modelled with a Lambertian reflectivity of 98% and 7.5% for the visible and UV ranges, respectively. Light diffusion from the lateral walls is dominated by TPB re-emission in the visible range, since the probability that a UV photon survives before absorption in the TPB (~100 μm thick) is negligible. The TPB is
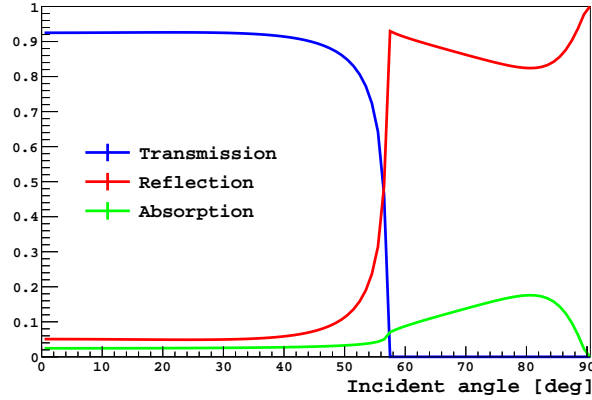
Figure 7. Coefficients of transmission, reflection, and absorption versus incident angle for ITO, when photons cross, in sequence, fused silica, ITO, and liquid argon.

assumed to re-emit a single visible photon for each absorbed UV photon[1] with a characteristic time of 1.5 ns [2].

The PMT cathodes are modelled as a dielectric, but with an arbitrarily reduced absorption length, in order to fully absorb the transmitted visible photons in a few micrometers. Absorbed photons are converted to photo-electrons, if they survive the PMT quantum efficiency cut which is a function of the wavelength.

All the remaining detector materials adopt standard Geant4 modelling, with parameters tuned by the DarkSide-50 data. The tuning procedure requires calibrations of the optical response of the detector before tuning the energy response. This ordering is required to break degeneracies between non-linearities in the LAr energy response and the non-uniformities in the photon collection efficiency. A key element for optical tuning requires identification of observables which are independent of energy and interacting particles, such as:

- photon collection efficiency as a function of the event position (collection efficiency);

- ratio of light collected on the top and on the bottom PMT arrays as a function of the vertex position in the drift direction (top/bottom ratio);

- fraction of S1 light observed by each PMT (S1 channel occupancy);

- fraction of S2 light observed by each PMT (S2 channel occupancy).

The reference sources used for the optical tuning are ^{39}Ar and ^{83m}Kr. ^{39}Ar is a beta emitter with a Q-value = 565 keV and $\tau_{1/2}$ = 269 y. It is produced by cosmic ray interactions with ^{40}Ar, and hence is present in atmospheric argon, which has an activity of ~1 Bq/kg [19]. The atmospheric

---

[1]V. M. Gehman *et. al.* [17] measured 1.2 visible photons emitted for each UV (128 nm) photon. This is not considered in this work because of the low significance of the measurement (σ~1.6).

[2]E. Segreto [18] found delayed light emission components from TPB. As this is a recent result it has not been included in G4DS. However, tuning of the LAr scintillation time profile almost entirely renormalizes the effect of any TPB delayed re-emission, as shown in Section 5.
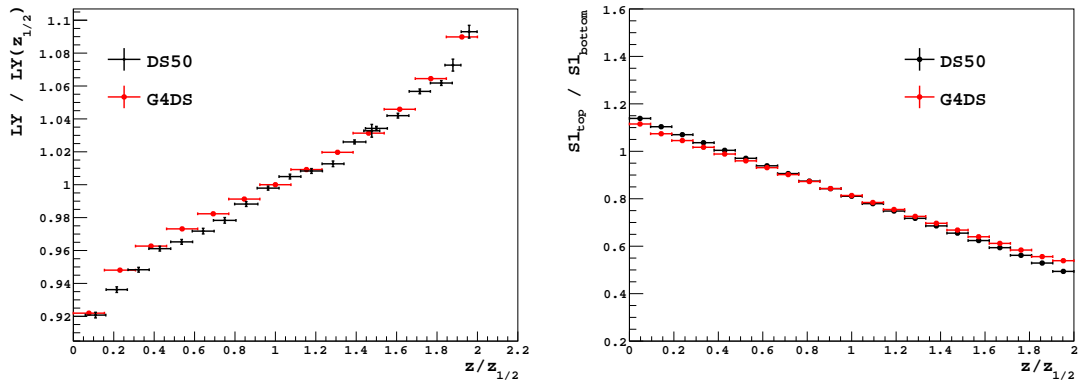
Figure 8. Relative light collection (left) and top-bottom ratio in light collection (right) as a function of the vertical position of the event. The normalization is relative to the center of the TPC, so that $z/z_{1/2} = 0$ corresponds to the top, $z/z_{1/2} = 2$ correspond to the bottom.

argon campaign in DarkSide-50 provides beta events that are uniformly distributed in the TPC. The isomeric state of ^{83m}Kr decays with a $\tau_{1/2} = 1.83$ h, emitting a fast ($\tau_{1/2} = 156$ ns) cascade of two 32.1 and 9.4 keV electrons, providing a clear and identifiable peak in S1. Gaseous ^{83m}Kr was injected directly into the TPC, and decayed into stable ^{83}Kr in few hours without affecting the radio-purity of the LAr.

The tuning is performed by generating simulation samples obtained by choosing optical parameters near their nominal values for comparison to dedicated DarkSide measurements or extracted from published literature. The large number of parameters led to a massive ($O(10^4)$) collection of simulation samples. The selected parameters were then determined by simultaneously minimizing the χ^2 of the four variables listed above.

With the above geometry the simulation underestimated the top/bottom ratio observed in the data, and the χ^2 minimization was unable to converge. This problem was resolved by introducing in the simulated geometry a condensed liquid argon layer (100 μm thick) on the underside of the top fused silica window, as quoted in Table 1. This is motivated by considering the possibility that the gas layer was condensing on the window, interfaced with LAr on the other side. An alternative explanation is that the layer represents an empirical correction for the TPB optical response to visible photons, based on a limited amount of data from lab measurements. The layer of condensed liquid argon provides additional total internal reflection between liquid and gaseous argon, and enhances the probability of photon collection in the top PMTs. The presence of this additional layer reduces the disagreement between the data and the MC simulation of the collection efficiency, and the top/bottom ratio as function of z-position to the sub-percent level, as shown in Figure 8.

The PMT channel occupancy is the best estimator testing the light collection as a function of the radius in the plane orthogonal to the electric field. The excellent agreement, at a few percent, between S1 data and G4DS for most of the PMTs was verified by the uniformly distributed ^{39}Ar events (see Figure 9).

S2 modelling has to also take into account the radial dependence of the S2 scintillation yield. This was measured in DarkSide-50 with ^{83m}Kr data, which can be selected by S1 cuts. The xy-position reconstruction, which is based on the S2 pattern on the top array of PMTs, allows extraction
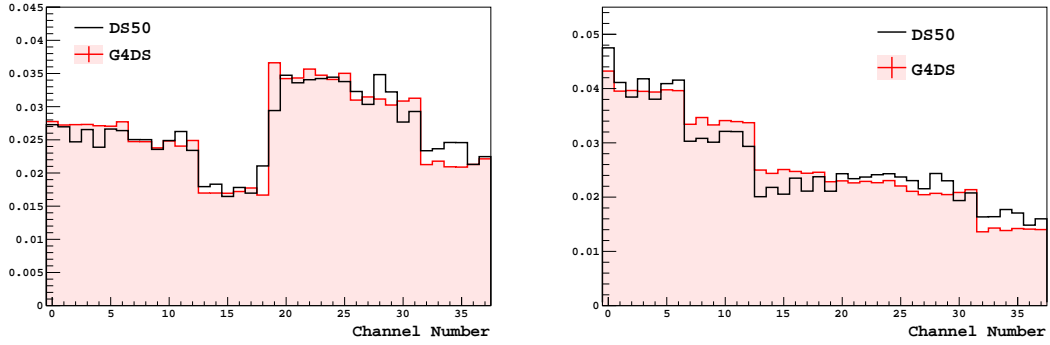
Figure 9. S1 (left) and S2 (right) channel occupancy comparisons between data and G4DS. Channels between 0-18 (19-38) correspond to the top (bottom) array of PMTs.

of the radial dependence of the S2 yield (Figure 10), and reveals a factor of ~4 difference between the S2 yield at the TPC center compared to the edges. This effect could be produced by a radial non–uniformity in the electric field in the gas region caused either by a deformation of the top window or a distortion of the grid, or a non-planarity of the grid or the liquid surface. Another potential cause could be non–uniformity of the condensed LAr layer thickness, on the lower surface of the top window. Once such effects are included in the simulation, the S2 channel occupancy in G4DS agrees with the data, as shown in Figure 9 (right), within a few percent for most of the PMTs.
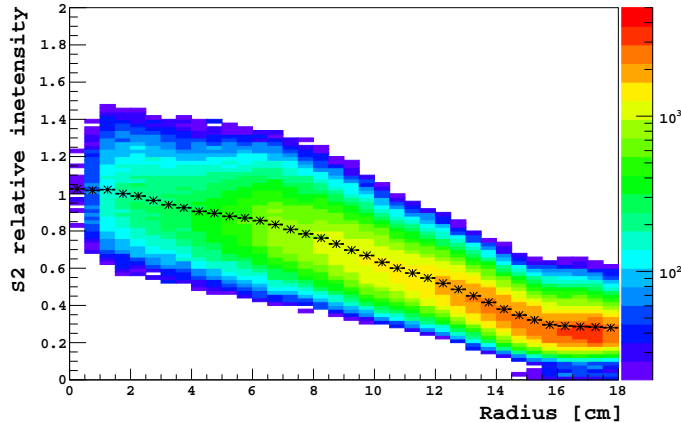

Figure 10. Radial dependence of the S2 relative yield, extracted from ^{83m}Kr. Black dots correspond to the mean S2 value at fixed radii.

Light propagation in LAr also depends on absorption and Rayleigh scattering. LAr absorption has a minimal impact since its characteristic absorption length (3.8±1.2 m from the tuning of G4DS) is much larger than the TPC size. On the other hand, DarkSide-50 is very sensitive to Rayleigh scattering, which is modelled in G4DS as function of the wavelength. The method is described in [20, 21]. The best fit to the data for the scattering length at 128 nm, is 46±11 cm, which is in agreement with 55 ± 5 cm obtained in reference [21] where the Rayleigh scattering length was extrapolated from measurements at higher wavelengths. However, it is in tension with a value of 66 ± 3 cm, which was directly measured at 128 nm [22], and a value of 90 cm that is obtained from

theoretical considerations [20].

5 The PARIS model for scintillation and ionization in liquid argon

The fine tuning of the TPC optical response as described in the previous section almost entirely resolves the degeneracies between the light collection in DarkSide-50 and the LAr S1 and S2 energy response, which was expected to be non–linear at non–null fields. G4DS adopts an effective model to parameterize the processes inducing the S1 and S2 signals. This model is called PARIS (Precision Argon Response Ionization and Scintillation), which is coded in a single Geant4 process class and relies on the fundamental principles governing the ionization and scintillation processes of LAr.

A fraction of the energy deposited by external radiation in noble liquids is converted into N_i electron-ion pairs, and in N_{ex} excited atoms. A residual fraction of energy is dissipated by heating, either by producing secondary nuclear recoils or inducing sub-excitation electrons. The combination of these heating processes are grouped under the name of quenching, and is dominant for nuclear recoils, where the quenching reduces the visible energy by a factor ~3-5 in LAr [23], but is negligible for electron recoils. It is assumed in PARIS that there is no quenching for electron recoils. Using this assumption, the energy deposited by an electron recoil, E_{dep}, is divided into excitation and ionization,

$$E_{dep} = N_i W_i + N_{ex} W_{ex}, \qquad (5.1)$$

where W_i and W_{ex} are the ionization and excitation work functions required to produce an ion-electron pair and an exciton, respectively. For simplicity, an effective work function, W, is introduced so that

$$E_{dep} = W(N_i + N_{ex}). \qquad (5.2)$$

Then defining $\alpha_k = N_{ex}/N_i$, where $k = \{ER, NR\}$ for electron and nuclear recoils respectively, the effective work function can be expressed as

$$W = \frac{\alpha_k W_{ex} + W_i}{1 + \alpha_k}. \qquad (5.3)$$

Consequently, the number of electron-ion pairs and excitons can be re-defined as

$$N_i = \frac{E_{dep}}{W} \frac{1}{1 + \alpha_k}, \qquad (5.4)$$

and

$$N_{ex} = \frac{E_{dep}}{W} \frac{\alpha_k}{1 + \alpha_k}. \qquad (5.5)$$

The value of W is fixed to 19.5 eV, as suggested by T. Doke *et al.* [24]. The excitation–to–ionization ratio α_{ER} is equal to 0.21 [24] for electron recoils and $\alpha_{NR}=1$ for nuclear recoils. Since α_{NR} can be fully absorbed by the nuclear recoil quenching function, any deviation from a true α_{NR} value is re-normalized by the quenching factor without loss of generality, as described in Subsection 5.3. When ions and electrons recombine, they produce excited atomic states, which

further contribute to the S1 component, and reduce the S2 component. Each S1 photon can then originate either directly from the excitation component, or from the recombination of electron-ion pairs. Under the assumption that each excitation and ionization quantum can generate only one photon, S1 can be parametrized as

$$S1 = g_1(N_{ex} + r(E) \times N_i), \tag{5.6}$$

where $r(E)$ is the recombination probability, as a function of the kinetic energy E, and g_1 is the collection efficiency of photons generated in liquid argon, including the PMT optical coverage and quantum efficiency, and the light absorption in the detector materials. g_1 was estimated equal to 0.157±0.001, by simulating UV photons uniformly distributed in the TPC. In a similar way, S2 is proportional to the number of free electrons, which survive recombination and are extracted into the gas pocket

$$S2 = g_2 Y_{S2} \times (1 - r(E)) \times N_i. \tag{5.7}$$

Here, g_2 (0.163±0.001) accounts for the detection efficiency of photons generated in the gas pocket and Y_{S2} is the electroluminescence yield. In G4DS, all electrons are assumed to recombine with ions under null field. With this assumption, S1 in Equation 5.6 can be expressed as

$$S1 = g_1(N_{ex} + N_i) = g_1 \frac{E_{dep}}{W}. \tag{5.8}$$

The above assumption is confirmed within 2% for energies between 40–670 keV by the Micro-CLEAN experimental results [25]. In the presence of an external electric field, electrons can escape the ion-pair cloud, reducing the recombination contribution to S1 signal and enhancing the S2 signal.. The probability of escaping the cloud depends on the cloud size, which is defined by the Onsager radius [26], and hence on the stopping power of the recoiling particle.

Several models have been developed to describe the recombination probability as functions of particle energy and electric field. Among these, Jaffe's theory [27] proposes diffusion equations for positive ions and electrons to explain the columnar recombination of ion-electron pairs around the particle track when subject to an external electric field. This model was tested with a ^{207}Bi source in LAr at different fields by E. Aprile *et al.* [28]. The Thomas-Imel box model [29] simplifies Jaffe's theory by assuming zero diffusion and zero ion mobility. This model matches the data in the regime of "short" tracks, *i.e.* when the track is shorter than the mean ionization electron–ion thermalization distance. This is shown by T. H. Joshi *et al.* [30] for ^{37}Ar in LAr. The Doke-Birks model [24], which is based on Birks' law, empirically parametrizes the recombination effect and was found to be in good agreement with data in the "long" track regime. M. Szydagis *et al.* [31] suggests an approach where both models are applied, after a regime selection. This method is embedded in a Geant4-based simulation code called NEST [31], and has been successfully applied in several liquid xenon experiments [32, 33].

The NEST approach combines the Thomas-Imel and Doke-Birks models, by constraining the associated parameters in several experimental data sets. Such sets are rather abundant for liquid xenon but limited to only a few energies for argon (see for instance [23, 28, 34–37]). The attempt to implement a NEST–like approach in G4DS suffers from the lack of LAr data, where the difficulty lies

in choosing when and how to transition between the two regimes. Thus PARIS embeds a simplified and effective model in order to reproduce only DarkSide-50 data. However as shown here, the extremely good agreement found between data and Monte Carlo, suggests that a generalization of the PARIS approach beyond DarkSide-50 is possible.

The essence of the PARIS approach is an empirical parametrization of the recombination probability, which depends on the kinetic energy of the ionizing particle. This probability is defined over the entire energy range for single scatter events, and takes the functional form

$$r(E) = \text{erf}(E/p_1)(p_2 \times e^{-E/p_3} + p_4), \tag{5.9}$$

where erf is the error function, E is the kinetic energy, and p_i, with i ranges from 1 to 4, are free parameters derived from the fit of DarkSide-50 data, as shown in the next subsection. The dependence on the electric field is not considered since Equation 5.9 was tuned only on for DarkSide-50 data with a 200 V/cm drift field.

The nuclear recoil energy is defined with respect to the electron recoil scale after the addition of a quenching factor independent of the electric field. In the Subsection 5.3, data and Monte Carlo comparisons are shown for different nuclear recoil quenching models. The quenching model in PARIS acts by scaling E_{dep}, and hence reducing the number of quanta, in Equations 5.4 and 5.5. The tension between the published results of nuclear recoil quenching in LAr, especially at low energies [38], suggests implementing the two most used models, the Lindhard [39] and Mei [40] models. A full description of quenching modelling in PARIS and the data vs. Monte Carlo comparison are shown in Subsection 5.3.

Statistical fluctuations of S1 and S2 are introduced in PARIS only at the photon emission level. In particular, it is assumed that each exciton and each recombined pair can induce exactly one photon. The number of emitted photons contributing to the S1 pulse is modelled with a Poisson distribution, with mean number equal to $N_{ex} + r(E)N_i$. Fluctuations in S2 are modelled by randomly generating photons with Poisson statistics distributed around Y_{S2} for each extracted electron (see Subsection 5.4). The optical properties of G4DS, described in the previous section and independently tuned on the energy response of DarkSide-50 to ^{39}Ar and ^{83m}Kr, naturally determine the light collection efficiencies g_1 and g_2 in Equations 5.4 and 5.5. The accurate determination of the detector response as a function of the energy and position of the event, is essential in order to test the robustness of the G4DS approach, as demonstrated in the following subsection.

S1 and S2 photons are emitted with Gaussian distributed wavelengths using μ=128 nm and σ=2.6 nm. Singlet and triplet de-excitation times are fixed to 6 ns and 1.6 μs, respectively. The population probability of the singlet or triplet state is determined by a singlet-to-triplet ratio, depending on the ionizing particle energy. This is tuned using calibration data (see Subsection 5.2). Electrons surviving recombination are drifted in the MC to the level of the liquid/gaseous argon interface with a velocity of 0.93 mm/μs. Drifted electrons undergo diffusion, with transverse and longitudinal components of 4.8 cm^2/s [41] and 18 cm^2/s [42], respectively. An electron drift lifetime of 15.8 ms, as measured by DarkSide-50 with ^{83m}Kr calibration data, is introduced to take into account the effects of impurities in LAr. Each electron is tracked along the drift path in the liquid, and the electron mobility in gaseous argon is fixed at 475 cm^2/s/volt [43]. At the liquid gas interface, the extraction and the electroluminescence fields are 2.8 kV/cm and 4.2 kV/cm,

respectively, and S2 photons are generated along the electron drift path in the gas pocket. The time difference between PMT detection of S2 photons and particle interaction is the composition of the electron drift times in LAr and in gas pocket, the de-excitation of the excited argon dimer, and the photon time of flight.

The following subsections discuss in detail the S1 and S2 energy response, the S1 time profile which is crucial for pulse shape discrimination between electron and nuclear recoils, and the quenching of the nuclear recoil energy.

5.1 The S1 response to electron recoils

The S1 response to electron recoils is derived from Equations 5.4, 5.5, and 5.6

$$S1 = g_1 \frac{E_{dep}}{W} \frac{r(E) + \alpha_{ER}}{1 + \alpha_{ER}}. \tag{5.10}$$

Ideally, the only undefined quantity in this equation is the recombination probability, $r(E)$, which requires tuning using the data. However, inaccuracies in TPC optical tuning can induce a small degeneracy between the collection efficiency g_1 and the effective work function W of Equation 5.3. A scaling factor, whose deviation from one is comparable with the inaccuracy in collection efficiency, is expected. Tuning of the recombination probability relies on the simultaneous fit of the energy spectra induced by the decays of ^{37}Ar, ^{83m}Kr, and ^{39}Ar (from the atmospheric argon run), which are present or artificially produced and distributed in the active mass. Cosmogenic ^{37}Ar decays via electron capture, emitting an X-ray of 2.62 keV with 8.4% Branching Ratio (BR). The ^{37}Ar sample used in this analysis was identified in early runs of the underground argon campaign, since it has a relatively short half life ($\tau_{1/2}$=35.5 d).

^{39}Ar is a unique first-forbidden β-decay, and the deviation of the spectral shape from an allowed β transition has to be taken into account using the shape factor.

$$F(T) = \left((T + m_e)^2 - m_e^2 \right) + (Q - T)^2. \tag{5.11}$$

Here T is the kinetic energy, and Q the Q-value, which is known with 1% accuracy. Uncertainties on the screening correction [44] and on the shape factor prevent us for calibrating the S1 response at low energies (< 10 keV) with ^{39}Ar. The low energy calibration thus relies on ^{37}Ar (2.62 keV) and on ^{83m}Kr (41.5 keV).

Calibration data for the three sources are selected by applying a fiducialization along the drift field (40 < drift time < 334.5 µs) to minimize the contamination from the ^{40}K, ^{238}U, and ^{232}Th from the PMT glass and stem, as done in the DarkSide-50 analyses for WIMP searches [4, 5]. Background subtractions are applied to the ^{37}Ar and ^{83m}Kr data, using data selected from periods where the source was not present or negligible.

For the ^{39}Ar sample, the uncertainties on the theoretical spectral shape impose a low energy threshold in the fit of this source conservatively set at 500 pe (~70 keV). We used the underground argon spectrum as background for the atmospheric ^{39}Ar sample. The only difference between the two, with the exception of the depletion in the ^{39}Ar contamination, is an additional ^{85}Kr contamination in the underground argon sample not observed in atmospheric argon [5]. This was estimated to be present with an activity of ~2 mBq/kg, about 0.2% of the ^{39}Ar rate in atmospheric argon and hence neglected in this work.
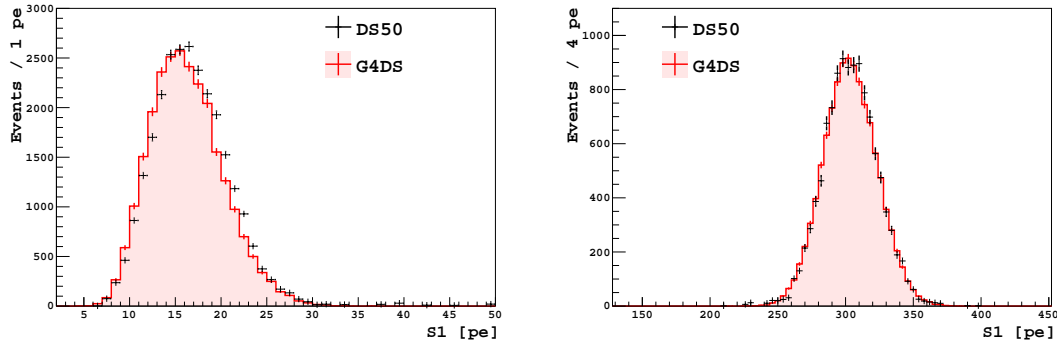
Figure 11. Comparison between data (black) and Monte Carlo (red) for ^{37}Ar (left) and ^{83m}Kr (right) S1 spectra.
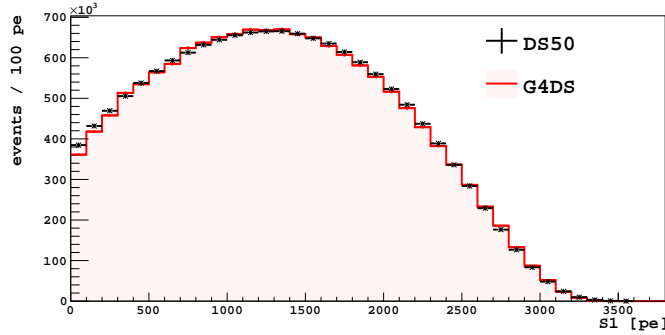

Figure 12. Comparison between data (black) and Monte Carlo (red) for the ^{39}Ar S1 spectrum. The energy region below 500 pe was not used to fit the energy scale, due to the uncertainties on the theoretical spectral shape.

The fit gives in a scaling factor of 1.01, which is applied to S1 to take into account inaccuracies in the photon collection efficiency. The comparisons between data and Monte Carlo are shown in Figures 11 and 12. No corrections are applied to the S1 resolution: the excellent agreement in the S1 resolution between data and Monte Carlo confirms the robustness of the PARIS approach and suggests that the photon emission process is dominated by Poisson statistics.

The parameters of Equation 5.9 obtained from the fit are $p_1 = 3.77$, $p_2 = 0.277$, $p_3 = 113$, and $p_4 = 0.665$ and the corresponding recombination probability is shown in Figure 13 (left) as function of the kinetic energy. At an electric field of 200V/cm, the light yield, defined as defined as S1/E (see Equation 5.10), has a maximum at ~15 keV with a value of ~7.6 pe/keV, and reaches a plateau at high energies equal to ~6 pe/keV (see Figure 13 right).

In addition to the use of diffuse sources in the TPC, two external sources, ^{57}Co and ^{133}Ba, were positioned in the liquid scintillator veto close to the cryostat. These were used to cross check the tuning of G4DS. The dominant gamma line emissions from ^{57}Co and ^{133}Ba are at 122 keV and 356 keV, respectively. These gammas have to cross a double–steel cryostat layer, the bath of liquid argon surrounding the TPC, and the TPC materials (teflon and rings of copper), before reaching the active
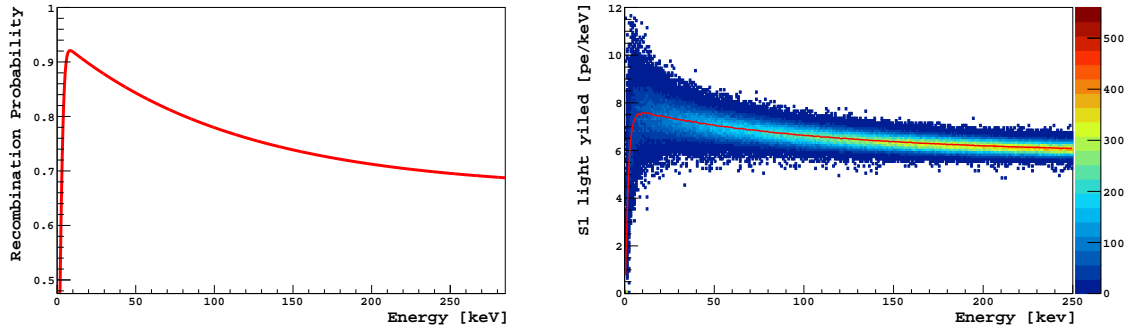
Figure 13. Recombination probability as a function of the particle energy, for single scattered events, extracted from DarkSide-50 data (left) and the G4DS light yield at 200 V/cm (right), defined as S1/E. The red curve in the right panel represents the mean light yield as function of the electron recoil energy.

volume. The non-uniformity in the position distribution of the induced electron recoils impacts the light collection efficiency, which is strongly dependent on the event position. Accurate calibrations of the optical properties and of the S1 response to uniformly distributed sources naturally overcome this issue.

Figure 14 shows the excellent agreement with the energy response of single scatter events. Since the experiment is designed to look for WIMPs which are also single scatter, this is a critical element for agreement. A small difference in the S1 response was expected for multiply scattered events, when the drift path of ionization electrons cross ion-electron pair clouds from a different interaction. Though this effect is not included in G4DS, the good agreement between Monte Carlo and the ^{57}Co and ^{133}Ba calibration sources for multiple scatter events, as shown in Figure 14, demonstrates that interference between ion-electron pair clouds is negligible for a drift field of 200 V/cm.
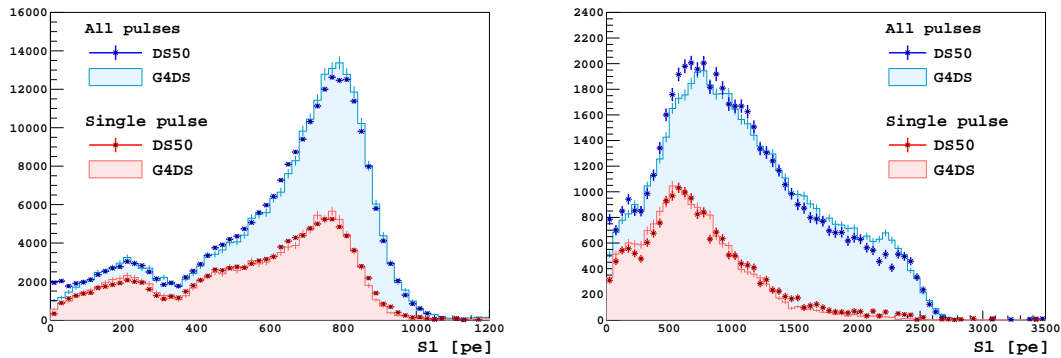

Figure 14. Single and multiple scatter S1 spectra of ^{57}Co (left) and ^{133}Ba (right) calibration sources in DarkSide-50 data, after background subtraction, and G4DS.

A further test on the validity of the PARIS model is provided by the ratio of g_1/W

$$\frac{g_1}{W} = \frac{S1}{E_{vis}},\tag{5.12}$$

where

$$E_{vis} = E_{dep}\frac{r(E) + \alpha_{ER}}{1 + \alpha_{ER}}.\tag{5.13}$$

The ratio, g_1/W, being independent of the field, allows to extrapolate the recombination effect at null field. In the limit case of $r(E)=1$, where
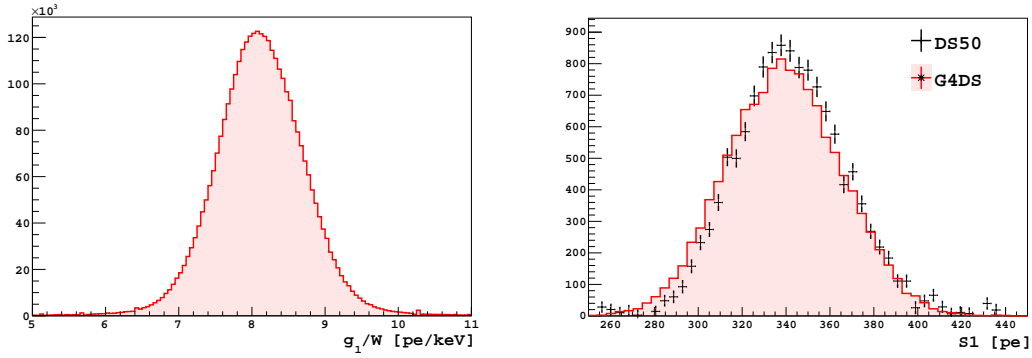
$$\frac{g_1}{W} = \frac{S1}{E_{dep}},\tag{5.14}$$

Figure 15. Left: g_1/W from the simulation of ^{39}Ar events at 200 V/cm. The mean value, 8.11 pe/keV, is in good agreement with the light yield, 8.1±0.2 pe/keV, measured at null field. Right: comparison of the S1 response to ^{83m}Kr between data and Monte Carlo at zero field.

G4DS predicts the light yield to be 8.11 pe/keV. Figure 15 shows the $S1/E_{vis}$ distribution of simulated ^{39}Ar decays at 200 V/cm (left) and the data/Monte Carlo comparison of ^{83m}Kr at null field (right). The measured value of 8.1±0.2 pe/keV in DarkSide-50 with a ^{83m}Kr source, after the correction for the z-dependence [5], is in excellent agreement with the G4DS prediction, suggesting that most of the electron-ion pairs recombine at null field. This extrapolation is, however, in conflict with the biexcitonic model [45] that predicts S1 quenching at null field due to electrons escaping the spatial distribution of ion-electron pairs along a particle track.

5.2 The S1 pulse shape profile

As already mentioned, the pulse shape profile is dominated by the characteristic de-excitation times of the singlet ($\tau_s \sim 6$ ns) and triplet ($\tau_t \sim 1.6$ μs) states of the argon dimers and by the probability to populate the various states. Electron recoils induce a slower pulse, since they mostly populate the triplet state, contrary to nuclear recoils which have a larger probability to populate the singlet state. Other sub-dominant effects affecting the pulse shape profile, like the TPB absorption-emission mechanism, the photon propagation, the electronics noise, and the PMT jitter are intrinsically provided by G4DS and by the electronics simulation.

The DarkSide-50 estimator for the S1 pulse shape discrimination, $f90$, is the ratio between the integral of the light pulse in the first 90 ns with respect to the total integration of up to 7 μs.

This ratio is simulated in G4DS by assigning each excited dimer to the singlet (triplet) state using a binomial distribution with probability p_s $(1 - p_s)$. The probability at 200 V/cm as function of the recoil energy, p_s, is derived for electron recoils using ^{39}Ar β decays and AmBe for nuclear recoils induced by scattered neutrons. The mean value of the $f90$ distribution was obtained by fitting this distributions for each 1–pe bin of S1 with the Hinkely model [46] and converted in the $p_s/(1-p_s)$ ratio ($f_{S/T}$) by fixing τ_s and τ_t to 6 ns and 1.6 μs, respectively. The comparisons between data and Monte Carlo in Figure 16 illustrate good agreement for $f90$ mean values for both nuclear and electron recoils.
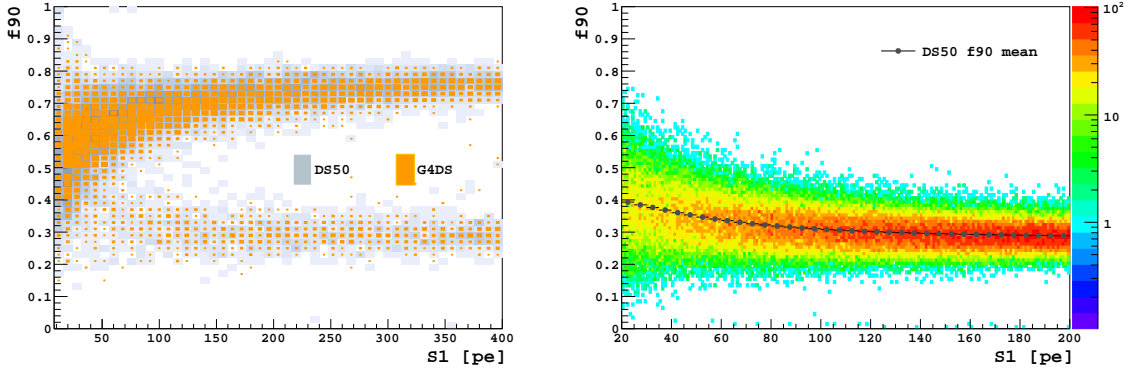

Figure 16. Left: $f90$ distribution as a function of S1 for the AmBe neutron source. Right: $f90$ vs S1 for simulated ^{39}Ar electron recoils compared with mean $f90$ extracted from the data.
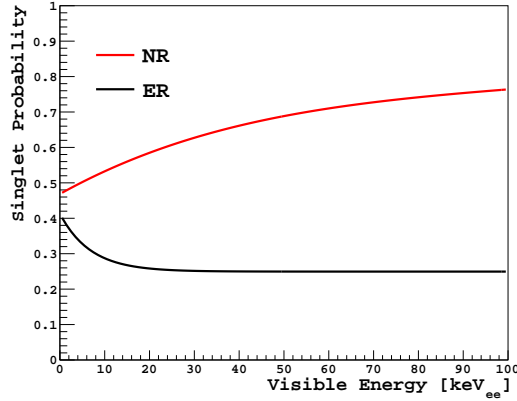

Figure 17. Singlet probability, p_s, for electron and nuclear recoils as a function of the visible energy at 200 V/cm drift field as coded in G4DS.

Figure 17 shows the extracted singlet probabilities for electron and nuclear recoils at 200 V/cm. The two $p_s(E)$ curves for electron and nuclear recoils are coded in the PARIS model. The relevant result of this work demonstrates the capability of G4DS to very accurately predict the electron recoil $f90$ statistical fluctuations, a key ingredient to define the WIMP acceptance band in the
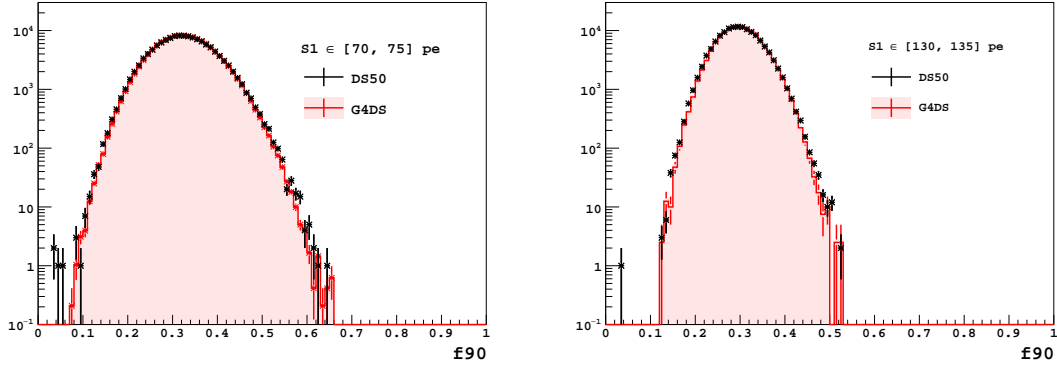
Figure 18. DarkSide-50 $f90$ distributions from the atmospheric argon campaign compared to G4DS simulations for S1 in [70, 75] pe (left) and [130, 135] pe (right) intervals. The selected sample includes single scatter events with a cut in the drift time within 40 μs and 330 μs.

DarkSide-50 experiment. The $f90$ distributions are shown in Figure 18 for two different S1 ranges, [70, 75] pe and [130, 135] pe, for the high statistics atmospheric argon data. In these two particular cases, the sample statistics count more than 10^5 events and correspond to ~20 years of DarkSide-50 operations with underground argon.

5.3 The quenching of nuclear recoils

The quenching factor in liquid argon (often called L_{eff} or scintillation efficiency[3]) was measured by SCENE [47], MicroCLEAN [48], WARP [49], and W. Creus *et al.* [50]. The four measurements agree within 2 σ with a value of approximately 0.28 at energies above 50 keV. At low energies, however, there is a tension between the SCENE data set, where L_{eff} decreases down to ~0.22 at 11 keV, and MicroCLEAN and W. Creus *et al.*, who observed an increase to 0.35 (15 keV) and 0.315 (16 keV), respectively.

In order to account for the nuclear recoil quenching, G4DS provides the option to switch between the Lindhard theory [39] and the D. M. Mei *et al.* [40] model, which modifies the Lindhard expression as follows

$$L_{eff}^M = L_{eff}^L \times \frac{1}{1 + k_B \frac{dE}{dx}}, \tag{5.15}$$

where L_{eff}^L is the Lindhard factor [39] and $k_B = 7.4 \times 10^{-4}$ MeV^{-1} g cm^{-2}.

Generally, L_{eff} is defined with respect to the electron recoil energy which is proportional to the deposited energy. It is usually extracted at null field, where all electrons and ions are assumed to recombine. Despite the fact that DarkSide-50 operated at 200 V/cm, accurate tuning of the recombination probability, as described above, allows one to constrain the L_{eff}.

---

[3]L_{eff} is usually defined with respect to the electron recoil light yield at null field at 122 keV, the gamma line emitted by ^{57}Co. The other definition for the quenching factor, the so-called Lindhard factor, is defined as the ratio between S1 and the nominal nuclear recoil energy at null field. In G4DS we confirm the linearity at null field for the electron recoil S1 energy scale, as observed by MicroCLEAN, at 2%. The two definitions provide the same information within this uncertainty.
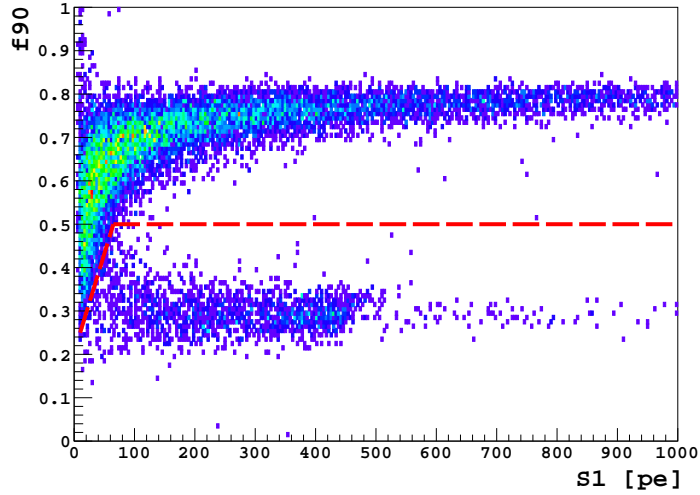
Figure 19. f90 vs S1 selection cuts to extract a pure sample of nuclear recoils from the AmBe calibration data. Same cuts were applied to the G4DS simulation of the AmBe source. See the text for more details.
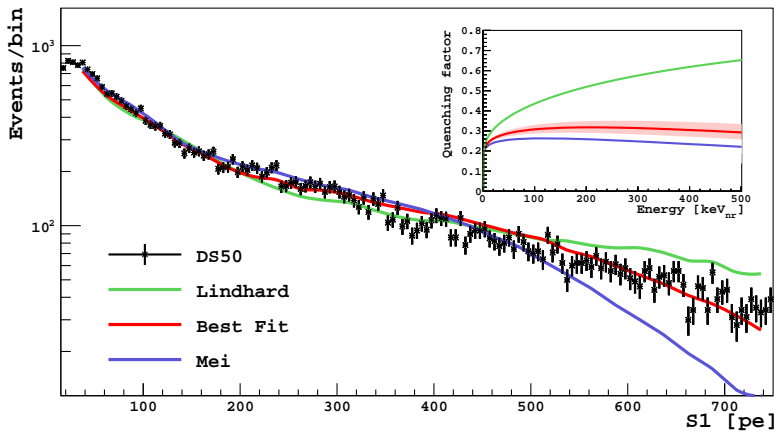

Figure 20. Data vs simulation comparison assuming the Mei and Lindhard models, and with the best fit of the k_B parameter in the modified Mei model.

Calibration data using a 10 Bq AmBe neutron source are used to select a sample of nuclear recoils, with a known energy distribution. AmBe emits neutrons in association with a 4.4 MeV gamma (BR of 65%) and coincident 4.4 MeV and 3.2 MeV gammas (BR of 3%). These events can be tagged by looking at the coincidence between the liquid scintillator detector and the TPC. The nuclear recoil data was further cleaned from low energy electron recoil signals in the TPC by applying a cut on $f90$. The cut, shown in Figure 19, was also applied to the simulated data set.

The comparison between DarkSide-50 data and G4DS with the Lindhard and the Mei models are shown in Figure 20. Both models are in tension with respect to data, as the Mei model underestimates the quenching factor, while the Lindhard model overestimates it. Since both models

were unable to reproduce the DarkSide-50 data, a modified Mei model is used as the default quenching model by fitting the single scatter nuclear recoil spectrum obtained from AmBe neutrons after freeing the k_B parameters. The fit converges for $k_B = 4.66^{+0.86}_{-0.94} \times 10^{-4}$ MeV^{-1} g cm^{-2}.

The result of the fit is shown also in Figure 21, where data sets from the literature are also compared. The so-obtained modified model is in good agreement with the SCENE and WARP measurements, and with the W. Creus *et al.* measurements above 20 keV. A slight variation at $\sim 2\,\sigma$ level arises when compared to the MicroCLEAN data set.
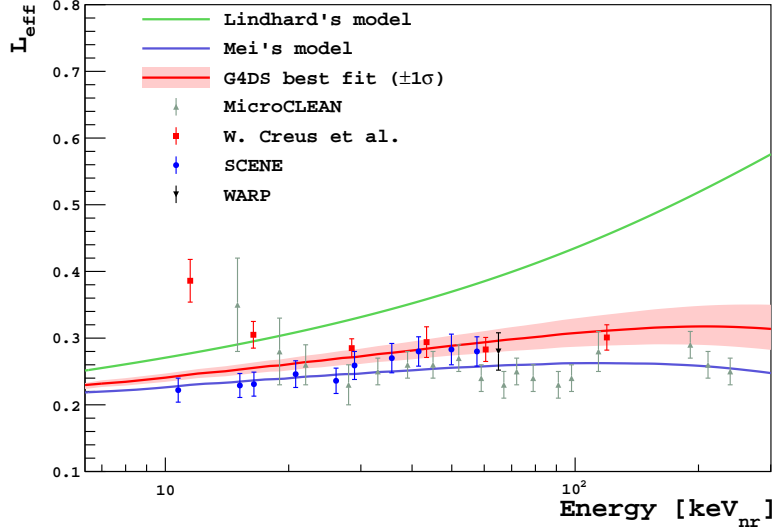

Figure 21. Comparison of the Lindhard and Mei models with the G4DS best fit of the DarkSide-50 data. SCENE [47], MicroCLEAN [48], WARP [49], and W. Creus *et al.* [50] data sets are also shown.

5.4 The S2 response

The S2 signal provides information on the number of scatters, the position, and energy of the interacting particle. The simulation of the S2 signal takes into account the dependencies of the optical response on the radial location of the event, which was discussed in Section 4. However, this requires tuning of the electroluminescence yield (Y_{S2}). More specifically, the number of photoelectrons detected in S2 is proportional to the number of ionization electrons which survive recombination and capture on impurities, and the number of emitted photons per electron is modelled with a normal distribution centered on Y_{S2} and with a resolution proportional to $\sqrt{Y_{S2}}$. The proportionality constant is a free parameter extracted from the calibration. The electroluminescence light is emitted uniformly along the electron drift in the gas pocket, whose duration is of the order of $\sim 1\,\mu$s, as observed in the data. We currently use the S1 parameters for the time response of S2; the limited role of the S2 time profile in the DarkSide-50 analyses makes the requirements on these parameters less severe.

Since S2 of ^{39}Ar events saturate the ADC above 5×10^4 pe, data were also acquired with a low-gain digitizer (CAEN V1724), which was placed with a CAEN V1720 during standard data acquisition. This allowed the detection of the S2 signal with a reduced amplification (factor of

~6) which avoided signal saturation. The radial dependence of S2, discussed in Section 4, is the main source of uncertainty in the S2 tuning. Figure 22 shows the good agreement between data and Monte Carlo for ^{39}Ar events in the central region (R_{xy}<12 cm). The mean value for Y_{S2} is 273 photons per extracted electrons, with $\sigma \sim 1.1 \times \sqrt{Y_{S2}}$. The averaged collection efficiency for a photon generated in the gas pocket is 0.163. The comparison in the outer shell (R_{xy}>12 cm) shows a discrepancy which is connected to the difficulty in measuring the radial correction at the TPC edges.
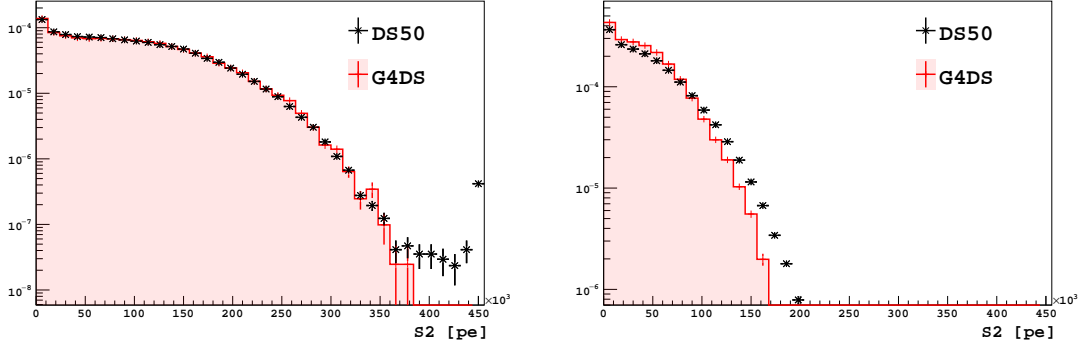

Figure 22. Data and G4DS comparison of the S2 response for ^{39}Ar events in the central column, R_{xy}<12 cm (left), and in the TPC outer shell, R_{xy}>12 cm (right).

A second test was performed by comparing data and simulated ^{83m}Kr events. However, these are not uniformly distributed in the LAr volume and have a strongly distorted S2 spectral shape. To mitigate this effect, events are simulated from the position distribution of the reconstructed data. Despite the fact that the simulated spectral shape does not fully match the data, the events fall in the same S2 range, and provide an interesting sample to test the correlation between S2 and S1. The observed good agreement is confirmed by ^{39}Ar data when selected in the central column, as shown Figure 23.
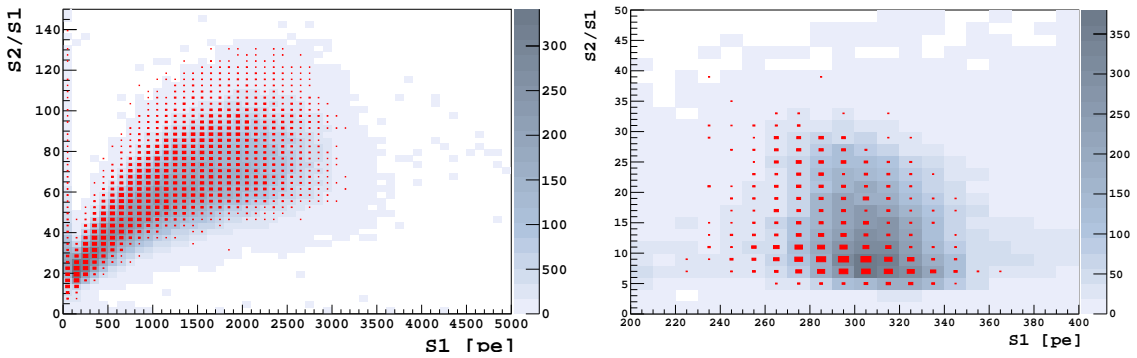

Figure 23. Data (grey scale) and G4DS (red boxes) comparison of the S2/S1 ratio versus S1 for ^{39}Ar events in the central column, R_{xy}<12 cm (left), and ^{83m}Kr generated with a spatial distribution derived from real data (right).

6 Conclusions

This work describes the DarkSide-50 simulation framework, G4DS, and its performance when compared with DarkSide-50 data. G4DS reproduces energy and time observables at the percent level. Such a precision was achieved mainly thanks to the careful tuning of the detector optical properties and to PARIS, the custom–made effective model describing the physical processes that produce the S1 and S2 signals. The comparisons with DarkSide-50 data presented in this work include nuclear recoil quenching, the S1 and S2 response at 200 V/cm drift field, and pulse shape discrimination. It is worth mentioning that G4DS is also able to precisely reproduce the detector resolution in S1, demonstrating the robustness of the approach.

G4DS has been widely exploited in several DarkSide-50 analyses, for example in the identification of the ^{85}Kr background, in the estimation of the ^{39}Ar depletion factor in underground argon [5], and in the prediction of the nuclear recoil background [4]. Furthermore, its modular and flexible structure allows an extension of G4DS to other detector geometries and physics cases under investigation for future experiments, such as DarkSide-20k [11], driving the technical design in order to maximize the light yield and the background discrimination power for the WIMP search, and ARGO [12], investigating the physics potential in the solar neutrino sector at the MeV scale. The recombination law in the PARIS model, in fact, remains valid at the MeV range, though the energy response strongly depends on the local density of ionization. This can differ starkly when going from minimum ionizing tracks, like those induced by neutrino elastic scattering off electrons, to nuclear recoils, as in the WIMP search. The accuracies of the PARIS model, demonstrated at few hundreds of keV with calibration sources, and of Geant4 electromagnetic processes, guarantee a comprehensive model, able to range from few keV to the MeV scale.

References

[1] LUX collaboration, D. S. Akerib et al., *Results from a search for dark matter in the complete LUX exposure*, *Phys. Rev. Lett.* **118** (2017) 021303, [1608.07648].

[2] PANDAX-II collaboration, Y. Yang, *Search for dark matter from the first data of the PandaX-II experiment*, in *Proceedings, 38th International Conference on High Energy Physics (ICHEP 2016): Chicago, IL, USA, August 3-10, 2016*, 2016. 1612.01223.

[3] E. Aprile et al., *First Dark Matter Search Results from the XENON1T Experiment*, 1705.06655.

[4] DARKSIDE collaboration, P. Agnes et al., *First Results from the DarkSide-50 Dark Matter Experiment at Laboratori Nazionali del Gran Sasso*, *Phys. Lett. B* **743** (2015) 456–466, [1410.0653].

[5] DARKSIDE collaboration, P. Agnes et al., *Results from the first use of low radioactivity argon in a dark matter search*, *Phys. Rev. D* **93** (2016) 081101, [1510.00702].

[6] S. Agostinelli, J. Allison, K. Amako, J. Apostolakis, H. Araujo, P. Arce et al., *Geant4: a simulation toolkit*, *Nucl. Instrum. Meth. A* **506** (2003) 250 – 303.

[7] DARKSIDE collaboration, P. Agnes et al., *The veto system of the DarkSide-50 experiment*, *JINST* **11** (2016) P03016, [1512.07896].

[8] DARKSIDE collaboration, P. Agnes et al., *The Electronics and Data Acquisition System for the DarkSide-50 Veto Detectors*, *JINST* **11** (2016) P12007, [1606.03316].

[9] T. Alexander, D. Alton, K. Arisaka, H. Back, P. Beltrame, J. Benziger et al., *Light yield in DarkSide-10: A prototype two-phase argon TPC for dark matter searches*, *Astropart. Phys.* **49** (2013) 44 – 51.

[10] S. Davini, P. Agnes, L. Agostino, I. F. M. Albuquerque, T. Alexander, A. K. Alton et al., *The darkside awakens*, *Journal of Physics: Conference Series* **718** (2016) 042016.

[11] C. E. Aalseth et al., *DarkSide-20k: A 20 Tonne Two-Phase LAr TPC for Direct Dark Matter Detection at LNGS*, 1707.08145.

[12] D. Franco, C. Giganti, P. Agnes, L. Agostino, B. Bottino, N. Canci et al., *Solar neutrino detection in a large volume double-phase liquid argon experiment*, *JCAP* **2016** (2016) 017.

[13] A. J. Koning, S. Hilaire and M. Duijvestijn, *TALYS-1.0*, *Proceedings of the International Conference on Nuclear Data for Science and Technology, April 22-27, 2007, Nice, France* (2008) 211.

[14] A. Ferrari, P. R. Sala, A. Fasso and J. Ranft, *FLUKA: A multi-particle transport code*, *CERN-2005-010, SLAC-R-773, INFN-TC-05-11* .

[15] T. Bohlen, F. Cerutti, M. Chin, A. Fasso, A. Ferrari, P. Ortega et al., *The FLUKA Code: Developments and Challenges for High Energy and Medical Applications*, *Nuclear Data Sheets* **120** (2014) 211–214.

[16] C. Green, J. Kowalkowski, M. Paterno, M. Fischler, L. Garren and Q. Lu, *The art framework*, *Journal of Physics: Conference Series* **396** (2012) 022020.

[17] V. Gehman, S. Seibert, K. Rielage, A. Hime, Y. Sun, D.-M. Mei et al., *Fluorescence efficiency and visible re-emission spectrum of tetraphenyl butadiene films at extreme ultraviolet wavelengths*, *Nucl. Instrum. Meth. A* **654** (2011) 116 – 121.

[18] E. Segreto, *Evidence of delayed light emission of tetraphenyl-butadiene excited by liquid-argon scintillation light*, *Phys. Rev. C* **91** (Mar, 2015) 035503.

[19] WARP collaboration, P. Benetti et al., *Measurement of the specific activity of ^{39}Ar in natural argon*, *Nucl. Instrum. Meth. A* **574** (2007) 83–88, [astro-ph/0603131].

[20] G. Seidel, R. Lanou and W. Yao, *Rayleigh scattering in rare-gas liquids*, *Nucl. Instrum. Meth. A* **489** (2002) 189 – 194.

[21] E. Grace and J. A. Nikkel, *Index of refraction, Rayleigh scattering length, and Sellmeier coefficients in solid and liquid argon and xenon*, 1502.04213.

[22] N. Ishida, M. Chen, T. Doke, K. Hasuike, A. Hitachi, M. Gaudreau et al., *Attenuation length measurements of scintillation light in liquid rare gases and their mixtures using an improved reflection suppresser*, *Nucl. Instrum. Meth. A* **384** (1997) 380 – 386.

[23] SCENE collaboration, H. Cao et al., *Measurement of Scintillation and Ionization Yield and Scintillation Pulse Shape from Nuclear Recoils in Liquid Argon*, *Phys. Rev.* **D91** (2015) 092007, [1406.4825].

[24] T. Doke, H. J. Crawford, A. Hitachi, J. Kikuchi, P. J. Lindstrom, K. Masuda et al., *LET Dependence of Scintillation Yields in Liquid Argon*, *Nucl. Instrum. Meth. A* **269** (1988) 291–296.

[25] W. H. Lippincott, S. B. Cahn, D. Gastler, L. W. Kastens, E. Kearns, D. N. McKinsey et al., *Calibration of liquid argon and neon detectors with* ^{83m}Kr, *Phys. Rev. C* **81** (Apr, 2010) 045803.

[26] L. Onsager, *Initial Recombination of Ions*, *Phys. Rev.* **54** (1938) 554–557.

[27] G. Jaffé, *On the Theory of Recombination*, *Phys. Rev.* **58** (Dec, 1940) 968–976.

[28] E. Aprile, W. H.-M. Ku, J. Park and H. Schwartz, *Energy resolution studies of liquid argon ionization detectors*, *Nucl. Instrum. Meth. A* **261** (1987) 519 – 526.

[29] J. Thomas and D. A. Imel, *Recombination of electron-ion pairs in liquid argon and liquid xenon*, *Phys. Rev. A* **36** (Jul, 1987) 614–616.

[30] T. H. Joshi, S. Sangiorgio, A. Bernstein, M. Foxe, C. Hagmann, I. Jovanovic et al., *First Measurement of the Ionization Yield of Nuclear Recoils in Liquid Argon*, *Phys. Rev. Lett.* **112** (May, 2014) 171303.

[31] M. Szydagis, N. Barry, K. Kazkaz, J. Mock, D. Stolp, M. Sweany et al., *NEST: a comprehensive model for scintillation yield in liquid xenon*, *JINST* **6** (2011) P10002.

[32] XENON100 collaboration, E. Aprile et al., *Dark Matter Results from 225 Live Days of XENON100 Data*, *Phys. Rev. Lett.* **109** (2012) 181301, [1207.5988].

[33] LUX collaboration, D. S. Akerib et al., *First results from the LUX dark matter experiment at the Sanford Underground Research Facility*, *Phys. Rev. Lett.* **112** (2014) 091303, [1310.8214].

[34] R. T. Scalettar, P. J. Doe, H. J. Mahler and H. H. Chen, *Critical test of geminate recombination in liquid argon*, *Phys. Rev. A* **25** (Apr, 1982) 2419–2422.

[35] S. Sangiorgio, T. Joshi, A. Bernstein, J. Coleman, M. Foxe, C. Hagmann et al., *First demonstration of a sub-KeV electron recoil energy threshold in a liquid argon ionization chamber*, *Nuclear Instruments and Methods in Physics Research Section A: Accelerators, Spectrometers, Detectors and Associated Equipment* **728** (2013) 69 – 72.

[36] A. Bondar, A. Buzulutskov, A. Dolgov, E. Grishnyaev, V. Nosov, V. Oleynikov et al., *Measurement of the ionization yield of nuclear recoils in liquid argon using a two-phase detector with electroluminescence gap*, *Journal of Instrumentation* **12** (2017) C05010.

[37] A. Bondar, A. Buzulutskov, A. Dolgov, L. Shekhtman and A. Sokolov, *X-ray ionization yields and energy spectra in liquid argon*, *Nuclear Instruments and Methods in Physics Research Section A: Accelerators, Spectrometers, Detectors and Associated Equipment* **816** (2016) 119 – 124.

[38] W. Creus, Y. Allkofer, C. Amsler, A. Ferella, J. Rochet, L. Scotto-Lavina et al., *Scintillation efficiency of liquid argon in low energy neutron-argon scattering*, *JINST* **10** (2015) P08002.

[39] J. Lindhard, M. Scharff and H. E. Schlott, *A model of nuclear recoil scintillation efficiency in noble liquids*, *Mat. Fys. Medd. K. Dan. Vidensk. Selsk.* **33** (1963) 1.

[40] D.-M. Mei, Z.-B. Yin, L. Stonehill and A. Hime, *A model of nuclear recoil scintillation efficiency in noble liquids*, *Astropart. Phys.* **30** (2008) 12 – 17.

[41] S. Amoruso, M. Antonello, P. Aprili, F. Arneodo, A. Badertscher, B. Baiboussinov et al., *Analysis of the liquid argon purity in the ICARUS T600 TPC*, *Nucl. Instrum. Meth. A* **516** (2004) 68 – 79.

[42] V. M. Atrazhev and I. V. Timoshkin, *Transport of electrons in atomic liquids in high electric fields*, *IEEE Transactions on Dielectrics and Electrical Insulation* **5** (Jun, 1998) 450–457.

[43] L. S. Miller, S. Howe and W. E. Spear, *Charge Transport in Solid and Liquid Ar, Kr, and Xe*, *Phys. Rev.* **166** (Feb, 1968) 871–878.

[44] A. Hime, *The MiniCLEAN Dark Matter Experiment*, *Proceeding of the DPF-2011* (Apr, 2011) .

[45] A. Hitachi, T. Doke and A. Mozumder, *Luminescence quenching in liquid argon under charged-particle impact: Relative scintillation yield at different linear energy transfers*, *Phys. Rev. B* **46** (Nov, 1992) 11463–11470.

[46] W. H. Lippincott, K. J. Coakley, D. Gastler, A. Hime, E. Kearns, D. N. McKinsey et al., *Scintillation time dependence and pulse shape discrimination in liquid argon*, *Phys. Rev. C* **78** (Sep, 2008) 035801.

[47] SCENE Collaboration collaboration, T. Alexander, H. O. Back, H. Cao, A. G. Cocco, F. DeJongh, G. Fiorillo et al., *Observation of the dependence on drift field of scintillation from nuclear recoils in liquid argon*, *Phys. Rev. D* **88** (Nov, 2013) 092006.

[48] D. Gastler, E. Kearns, A. Hime, L. C. Stonehill, S. Seibert, J. Klein et al., *Measurement of scintillation efficiency for nuclear recoils in liquid argon*, *Phys. Rev. C* **85** (Jun, 2012) 065811.

[49] R. Brunetti, E. Calligarich, M. Cambiaghi, F. Carbonara, A. Cocco, C. D. Vecchi et al., *WARP liquid argon detector for dark matter survey*, *New Astronomy Reviews* **49** (2005) 265 – 269.

[50] W. Creus, Y. Allkofer, C. Amsler, A. D. Ferella, J. Rochet, L. Scotto-Lavina et al., *Scintillation efficiency of liquid argon in low energy neutron-argon scattering*, *JINST* **10** (Aug., 2015) P08002.